UC Davis
UC Davis Previously Published Works

Title
Proton-mediated reversible switching of metastable ferroelectric phases with low operation voltages

Permalink
https://escholarship.org/uc/item/5n26s858

Journal
Science Advances, 9(21)

ISSN
2375-2548

Authors
He, Xin
Ma, Yinchang
Zhang, Chenhui
et al.

Publication Date
2023-05-24

DOI
10.1126/sciadv.adg4561

Peer reviewed

eScholarship.org Powered by the California Digital Library
University of California

PHYSICAL SCIENCES

Copyright © 2023 The Authors, some rights reserved; exclusive licensee American Association for the Advancement of Science. No claim to original U.S. Government Works. Distributed under a Creative Commons Attribution NonCommercial License 4.0 (CC BY-NC).

Proton-mediated reversible switching of metastable ferroelectric phases with low operation voltages

Xin He[1,2], Yinchang Ma[2], Chenhui Zhang[2], Aiping Fu[3], Weijin Hu[4,5], Yang Xu[1], Bin Yu[1], Kai Liu[6], Hua Wang[1]*, Xixiang Zhang[2]*, Fei Xue[1,2]*

The exploration of ferroelectric phase transitions enables an in-depth understanding of ferroelectric switching and promising applications in information storage. However, controllably tuning the dynamics of ferroelectric phase transitions remains challenging owing to inaccessible hidden phases. Here, using protonic gating technology, we create a series of metastable ferroelectric phases and demonstrate their reversible transitions in layered ferroelectric α-In_2Se_3 transistors. By varying the gate bias, protons can be incrementally injected or extracted, achieving controllable tuning of the ferroelectric α-In_2Se_3 protonic dynamics across the channel and obtaining numerous intermediate phases. We unexpectedly discover that the gate tuning of α-In_2Se_3 protonation is volatile and the created phases remain polar. Their origin, revealed by first-principles calculations, is related to the formation of metastable hydrogen-stabilized α-In_2Se_3 phases. Furthermore, our approach enables ultralow gate voltage switching of different phases (below 0.4 volts). This work provides a possible avenue for accessing hidden phases in ferroelectric switching.

INTRODUCTION

Ferroelectric phase transitions exhibit intriguing physics including changes in the structural symmetry or polar ordering, which offers promising applications in information storage. To date, many approaches have been documented for enabling ferroelectric phase transitions to explore polar physics and device implications (*1*–*11*). For example, when the temperature exceeds an important value (i.e., the Curie point), ferroelectric-to-paraelectric transitions can occur; furthermore, the material concurrently undergoes structural evolution from noncentrosymmetric crystals with off-centered ions to centrosymmetric counterparts (*12*–*15*). Similarly, modifying the film thicknesses can induce phase/structural transitions because of the competition between polarization and depolarization fields: Thicker films retain ferroelectric phases, while thinner films without any compensation strategy easily become paraelectric (*16*–*18*). Moreover, the application of an electric field is another common method for triggering ferroelectric phase transitions, by which parallel (i.e., ferroelectric) and antiparallel (i.e., antiferroelectric) polar ordering can be reversibly switched (*2*, *6*, *19*–*21*). Despite multiple attempts to explore ferroelectric phase transitions, their "hidden" or intermediate phases, which contain rich physics, are still inaccessible on equilibrium phase diagrams.

Among various approaches to incite ferroelectric phase transitions, only the application of an electric field provides promise for developing memory devices with high performances (e.g., 10^{12} endurance and 10-ns operation speed) (*22*–*24*). However, these devices generally have only two digital resistance states owing to the lack of polar configurations beyond parallel/antiparallel ordering. In principle, a greater number of polar configurations offer broader possibilities for implementing multilevel, analog memory devices toward data-centric computing use (*25*–*28*). Accordingly, a strategy that can yield ferroelectric phase transitions with accessible, multiple polar phases (or hidden phases) is both fundamentally interesting and technologically important.

Using protonic gate technology as an efficient approach, we demonstrate reversible ferroelectric phase transitions among multiple metastable protonic α-In_2Se_3 phases in a transistor architecture [note S1 for the discussion over the van der Waals (vdWs) ferroelectric α-In_2Se_3]. Gate control over proton injection/extraction can render ferroelectric phase transitions between proton-sufficient and proton-deficient compounds (i.e., α-$In_2Se_3H_y$, α-$In_2Se_3H_x$, and α-$In_2Se_3H_i$; $y > x > i$). Piezoelectric force microscopy (PFM) mappings demonstrate that the proton-mediated phase transition indeed comprises a multitude of intermediate phases, arising from different protonation levels. Along with additional electrical measurements and first-principles calculations, we find that these created phases remain metastable and polar, which results in our observed volatile gate-tuning effect and hysteresis in drain-source curves. Moreover, our approach can enable ultralow gate voltage (<0.4 V) switching of ferroelectric phases, thus opening a promising avenue for developing low-power multilevel switching memory devices.

[1]ZJU-Hangzhou Global Scientific and Technological Innovation Center, School of Micro-Nano Electronics, Zhejiang University, Hangzhou 311215, China. [2]Physical Science and Engineering Division, King Abdullah University of Science and Technology, Thuwal 23955-6900, Saudi Arabia. [3]College of Chemistry and Chemical Engineering, Qingdao University, Qingdao, 266071, China. [4]Shenyang National Laboratory for Materials Science, Institute of Metal Research, Chinese Academy of Sciences, Shenyang 110016, China. [5]School of Materials Science and Engineering, University of Science and Technology of China, Shenyang 110016, China. [6]Physics Department, Georgetown University, Washington, DC 20057, USA.
*Corresponding author. Email: xuef@zju.edu.cn (F.X.); daodaohw@zju.edu.cn (H.W.); xixiang.zhang@kaust.edu.sa (X.Z.)

RESULTS

Device structure, calculations, and mechanisms

As previously reported (*29*, *30*), we implemented protonic gate technology in a three-terminal transistor architecture (Fig. 1A). This technology is used to manipulate the electronic and magnetic properties of certain materials (*30*–*35*), because protons (H^+) are the smallest ionic defects that can easily diffuse into rigid materials and achieve the desired tuning. The penetration of protons into

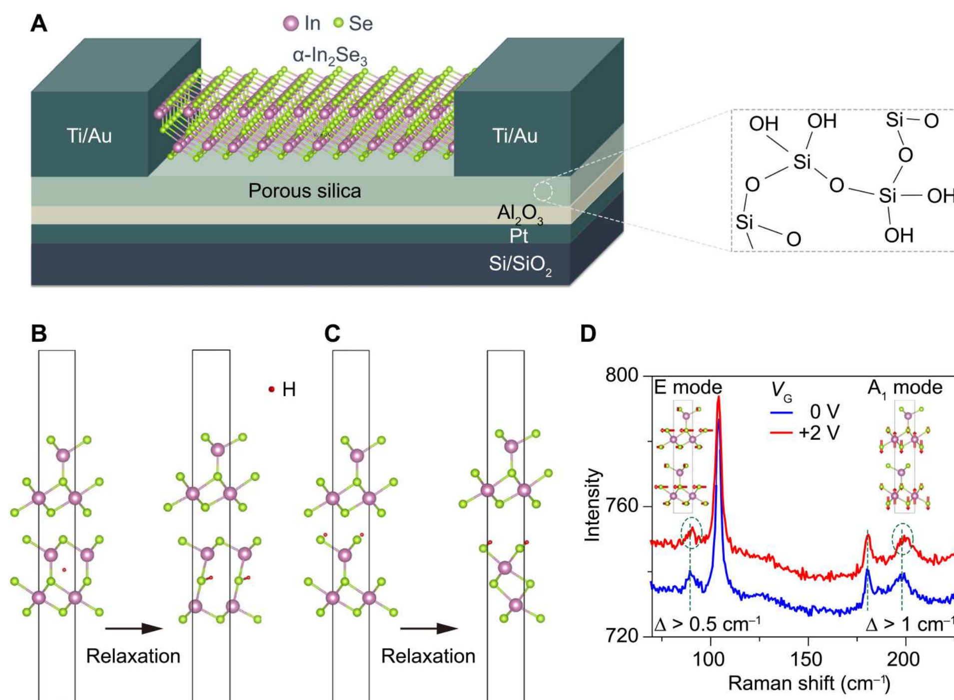

Fig. 1. Device structure and working principle. (**A**) Schematics of our three-terminal α-In_2Se_3 devices. Exfoliated α-In_2Se_3 flakes were placed on stacked heterostructure gates, which are composed of Pt, Al_2O_3, and porous silica. Right: The chemical structure of porous silica. First-principles structural relaxation of protonic α-In_2Se_3: H atom (**B**) at the intralayer and (**C**) at the vdWs gap. (**D**) Raman spectra under 0- and +2-V gate biases. Dashed circles highlight a blue shift of Raman peaks, which are enhanced by the proton injection across the vdWs gaps. For E and A_1 modes, schematics of calculated in-plane and out-of-plane phonon vibrations are shown in the inset, respectively.

channel materials has been confirmed by various measurement methods (*29*, *31*), thus proving the effectiveness of this strategy. In transistors, porous silica serves as a gate dielectric and essentially provides protons via the formation of Si-OH across the films or via the electrolysis of absorbed water into H^+ within silica (see note S2 and fig. S1 for more details) (*29*). Before coating 190-nm-thick silica films, we deposited high-quality Al_2O_3 insulator films (10 nm) on bottom Pt gate electrodes to prevent the breakdown of the transistor dielectric.

Exfoliated ferroelectric α-In_2Se_3 multilayers (typically ~20 to 60 nm) were transferred onto Pt/Al_2O_3/porous silica substrate. Gate control biases are applied using Pt electrodes and can accelerate proton diffusion, whereas the bias polarity determines proton injection or extraction (note S3). Because of proton concentration difference and room temperature thermal activation (*36*, *37*), certain protons within the silica films can naturally diffuse into ferroelectric α-In_2Se_3, making pure initial phase in the device channel protonic (α-$In_2Se_3+xH^++xe^-\leftrightarrow$α-$In_2Se_3H_x$), particularly at the bottom portion. Despite the top portion remaining less protonated, a hybrid compound (i.e., α-$In_2Se_3H_x$) can form with a proton concentration gradient perpendicular to its surface. To clarify the structure and stability of this compound, we used first-principles calculations and Raman spectroscopy (Fig. 1, B to D).

In theoretical calculations, we considered the protonation effect in multilayered α-In_2Se_3 (e.g., bilayer), which is based on an ideal, high-density hydrogen model: each α-In_2Se_3 unit cell is intercalated by one H atom. The energy barrier for injecting H atoms into the pure α-In_2Se_3 phase is ~200 meV, predicted by the minimum energy pathways of the protonation from climbing image nudged elastic band calculations (fig. S2). In principle, a higher density of H atoms leads to a strong electrostatic interaction between them, which can, in turn, increase the energy required to inject H atoms. It is worth noting that the experimental hydrogen density shall be smaller than that in our calculations. Therefore, the actual energy barrier is much lesser than 200 meV and can be easily overcome by applying an electric field, thus facilitating channel protonation, as described here. As shown in Fig. 1B, a single H atom is placed in the bottom intralayer of a bilayer α-In_2Se_3 unit cell (intralayer protonation) other than the top intralayer. The most energetically favorable structure is that H atoms reside near the middle Se atom layer and only chemically bond with this Se layer because there is charge transfer from the Se atom to the H atom (fig. S3). Simultaneously, intralayer sliding between central Se and H atoms occurs due to the small, generalized stacking fault energy for entirely shifting In-Se covalent bonds. After structural relaxation, the protonation at the bottom quintuple-atom-layer shows no obvious impact on the top quintuple-atom-layers (i.e., no proximate effect) because of the weak vdWs interactions. The crystal structure can relax to a metastable state: Once the H atom is removed, the unit cell reverses to the initial α-In_2Se_3 structure, while, with the presence of the H atom, it remains stable. Unexpectedly, the metastable phase exhibits noncentrosymmetric properties and holds both in-plane and out-of-plane dipoles. This signifies the existence of ferroelectricity, which originates from the structural asymmetry between the Se-H interaction and two adjacent In atoms.

Considering hydrogen migration from the bottom to the top, the scenarios of H atoms located at the vdWs gaps (interlayer protonation) are also theoretically examined (Fig. 1C and fig. S4). Because of the weak vdWs bonding and the low ground state energy for interlayer protonation, hydrogens are more energetically favorable to reside within the gaps. The protonated structures partially resemble β-In_2Se_3 but display in-plane and out-of-plane dipoles arising from the protonic Se atoms. On the basis of these calculated results, we conclude that, for a multilayer sample (>2 layers), the lower quintuple-atom-layers can be fully protonic but the upper layers may remain intact, resulting in created intermediate phases. Therefore, the zero proximity effect of protonation on neighboring layers ensures that numerous ferroelectric intermediate states (α-In_2Se_3H) can be created by slightly adjusting hydrogen concentrations and protonic thicknesses. Note that these multiple phases play a crucial role in the implementation of multilevel-resistance memory devices toward brain-inspired computing.

After the theoretical discussion over protonic structures, we move to the Raman characterization of protonic α-In_2Se_3 phases. Upon applying 0- and +2-V gate biases, the compound is subjected to different levels of protonation in which higher voltages impart a higher degree of protonation. As shown in Fig. 1D, we observe a blue shift for two prominent Raman peaks located at around 90 cm^{-1} (i.e., E mode) and 198 cm^{-1} (i.e., A_1 mode), whereas no shift is discerned for the other two peaks at 104 and 180 cm^{-1}, respectively. The shifted Raman modes may be originated from specific interlayer shearing and breathing vibrations, which are enhanced by proton injection across the vdWs gaps. The intralayer breathing modes corresponding to unshifted peaks are much less sensitive to the proton injection as shown in fig. S5. It is worth mentioning that the detected shift (>0.5 cm^{-1}), although small, can be reliably captured by our Raman measurement with a resolution of 0.5 cm^{-1}. These results provide strong direct evidence for protonation across the channel.

Multiple protonic phases

Schematics of ferroelectric protonation levels, with different gate biases, are presented in Fig. 2A. When considering a gate bias of 0 V, a few protons can spontaneously intercalate into multilayered channels, forming an α-$In_2Se_3H_{x1}$ compound. Following previous works (*29*, *31*), the bottom portion is inevitably protonated, while the top portion is only weakly protonated (as shown by the red dots in Fig. 2A). Upon applying a large positive gate bias, the whole channel becomes heavily protonated; thus, α-$In_2Se_3H_{x1}$ transforms into α-$In_2Se_3H_y$ ($y > x1$). Subsequently, as the gate bias is successively reduced to 0 and then to a negative value, the number of protons across the channel eventually decreases to ~0 because of the electric field–driven deprotonation (*29*). In this scenario, protons are gradually extracted from the channel with the assistance of a concentration gradient field (*38*), leading to a decreased proton population but still with a concentration gradient, decreasing from the channel's bottom surface to the top. Furthermore, in response to proton removal, the proton-sufficient α-$In_2Se_3H_y$ phase returns to proton-moderate α-$In_2Se_3H_{x2}$ at a gate bias of 0 V or proton-deficient α-$In_2Se_3H_i$ at a negative bias. It is noted that, in such a changing trend of gate biases, α-$In_2Se_3H_{x1}$ and α-$In_2Se_3H_{x2}$ have different protonation levels. In short, a large negative bias allows protons to be progressively driven out of the channel, resulting in the recovery of barely protonated phases (i.e., proton-deficient α-$In_2Se_3H_i$).

We used electrical hysteresis loops and in situ PFM to examine proton-induced ferroelectric phase transitions in single-domain channels. As per I_{DS}-V_G transfer curves, our fabricated protonic transistors can be phenomenologically classified into two groups: The first is shown in Fig. 2B, with gaps at the interface (Device 1), whereas the second is displayed in the following section, without gaps at the interface (Device 2). To avoid the influence of electric field–induced polarization switching in these channels, a small voltage was used to read drain-source currents and monitor phase transitions. In the case of Device 1, there are gaps (see inset of Fig. 2B) introduced by the rough silica surface (fig. S6) and sample transfer at the silica/sample interface, which greatly restricts the efficiency of proton insertion at a given gate bias. Therefore, a gradual current change and corresponding small slope (rather than an abrupt change and large slope) in the I_{DS}-V_G transfer curves are observed (Fig. 2B). When increasing gate biases, the drain-source current increases, which is attributed to two coupling effects: electrochemical doping from proton injection (supported by the band structure calculations in fig. S7) and protonated phase changes, which is consistent with previous works (*29*–*31*, *39*). The predominant reason is not likely associated with electrostatic electron injection (*40*) because the generated nonvolatile characteristics contrast with our volatile results to be discussed in the next section. As systematically illustrated in Fig. 2A, the hysteresis of Fig. 2B should be attributed to different protonation levels across the channel. For example, a 0-V gate bias acquired from either raising gate biases or lowing gate biases can lead to disparate protonated phases. It is worth mentioning that $V_G \leq 3$ V in Fig. 2 (B and C) cannot result in the dipole flipping of all α-In_2Se_3 protonic phases.

With small bias (0.5 V) sweeping, a hysteresis loop can unexpectedly appear (Fig. 2B), indicating the existence of a protonic phase in the channel. As the sweeping biases are progressively raised, the hysteresis becomes larger, which suggests that more protons move across the channel. We note that protonic hysteresis contrasts with that of electric field–tuned ferroelectric devices (*41*, *42*), which are always accompanied by an opening process (the hysteresis is only observed beyond certain threshold voltages). In addition, it is found that sweeping speed has a small influence on hysteresis (fig. S8).

To elucidate the phase transition with respect to hysteresis currents, we performed in situ PFM mapping over a full sweeping cycle from −3 to +3 V and then back to −3 V. PFM is a reliable and powerful tool to monitor phase transitions via amplitude mapping. The brightness of PFM amplitude signal can be used to indicate the protonation levels of the channel because the compound α-In_2Se_3H with different proton concentrations can exhibit different electromechanical responses (i.e., PFM amplitude). As shown in Fig. 2C and fig. S9A, there are uniform PFM responses across the channel, manifesting the presence of a single ferroelectric domain. Under different gate biases, the channels (marked by black dashed lines) display a spectrum of PFM amplitudes, which range from the response brighter to darker than the substrate. This is strong evidence for gate bias–dependent protonation that typically proceeds from the channel bottom surface to the top. Meanwhile, similar PFM images, particularly in the case of +2 to +3 V in Fig. 2C, demonstrate a trend of saturated protonation levels. Overall, a large positive gate bias ensures a high proton concentration across the channel, which facilitates heavy protonation; however, a small positive gate bias leads to light protonation.

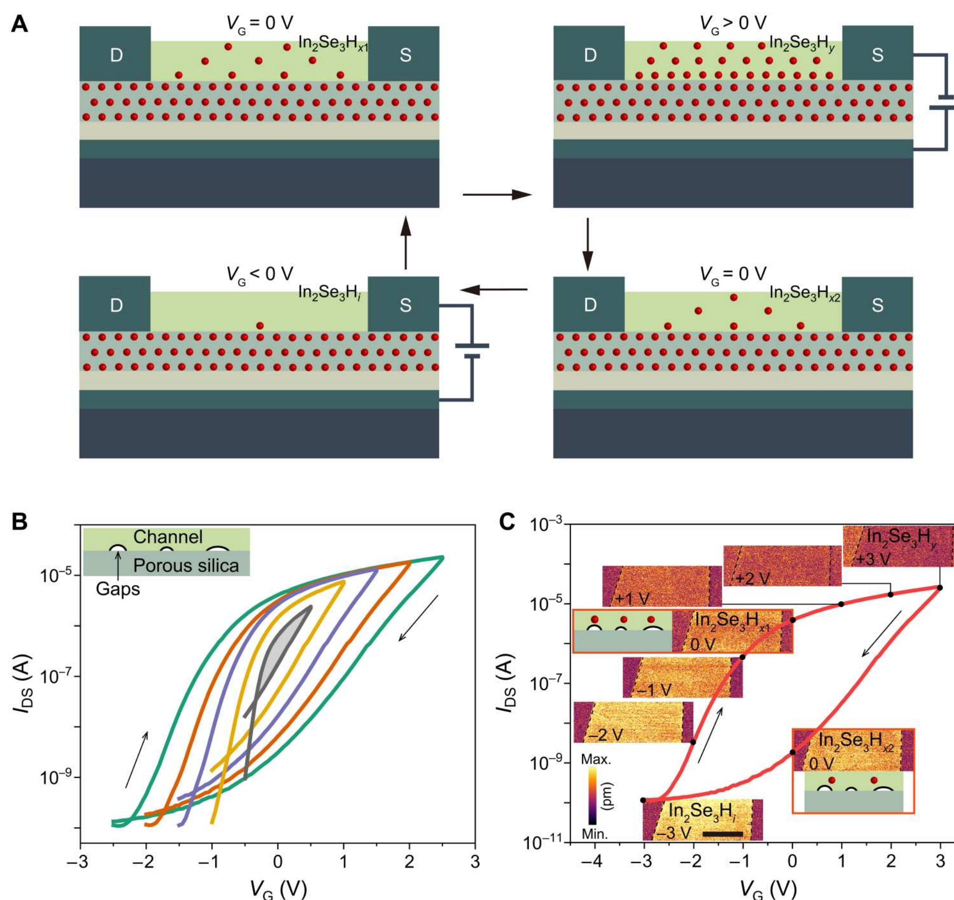

Fig. 2. Reversible switching of multiple ferroelectric phases by a protonic gate for Device 1. (**A**) Schematic working principle of ferroelectric phase transitions under different gate biases. Red dots in the porous SiO_2 layer represent protons. At a 0-V gate bias, thermal activation leads to an inherent proton penetration into the channel, forming the α-$In_2Se_3H_x$ compound. When applying a large, positive gate bias, plenty of protons (red dots) are pushed into the channel, achieving heavy protonation across the channel (i.e., α-$In_2Se_3H_y$ phase). Afterward, when the gate bias is returned to 0 V, protonation still exists but to a lesser content than that in the top left. As the gate bias becomes negative, protons can be driven out of the channel, and the composition returns to one close to the primary α-In_2Se_3 phase (i.e., α-$In_2Se_3H_i$). (**B**) Electrical hysteresis with respect to maximum gate biases. The first maximum voltage starts at 0.5 V and then increases in a 0.5-V step. The inset shows interfacial contacts between porous silica and the channel. (**C**) Phase evolution as a function of gate bias sweeping. PFM amplitude mappings, at the gate biases of −2, −1, 0, +1, +2, +3, 0, and −3 V, demonstrate the evolution of ferroelectric phases (rather than polarization switching) between proton-sufficient α-$In_2Se_3H_y$ and proton-deficient α-$In_2Se_3H_i$. For α-$In_2Se_3H_x$ compounds, schematic proton distributions are shown to differentiate their discrepancies. The α-In_2Se_3 channel is highlighted by black dashed lines. Note that $V_G \leq 3$ V here is insufficient to reverse the polarization of protonated α-In_2Se_3. Scale bar, 2 μm.

Furthermore, as shown in fig. S9B, we do not observe proton-induced sample height variations even at the gate biases of +3 and −3 V. By contrast, for gate biases of >5 V, marked structural changes are accompanied by a large bump in the topographical profile (fig. S10). These observations can be explained by the presence of a gate bias threshold for proton-triggered lattice expansion (*43*, *44*). Gate bias–dependent protonation can enable a multitude of intermediate ferroelectric phases and thus facilitate the implementation of multilevel memory devices with massive storage capacity (*45*), which are promising for neuromorphic computing hardware.

Volatile, gate-tuned protonic phases

Having established the concept of protonic ferroelectric phase transitions using a single domain model, we herein look to the effect of protonation on multidomain phases. As shown in Fig. 3A, outer and inner patterns outlined by black dashed lines were written by applying −8 and +8 V onto PFM probes, respectively, leading to a change in PFM response. Such voltage poling enforces protonic α-$In_2Se_3H_x$ compound to orient outward and inward such that a multidomain phase is acquired. However, once a large negative gate bias (−3 V) was applied, proton extraction immediately takes place, leaving a barely protonated phase (i.e., proton-deficient α-$In_2Se_3H_i$). This can be inferred from distinct responses of the PFM amplitude and phase in Fig. 3B. Note that, irrespective of domain orientations at a 0-V gate bias, proton extraction driven by a −3-V gate bias makes the entire channel reverse to the proton-deficient phase, producing almost identical PFM responses for both inner and outer patterns. Multidomain switching in Fig. 3A originates from the H atom shift. The multidomain is at a high-energy state and extremely sensitive to proton perturbation and thus can collapse with a proton-extracted bias (e.g., −3 V). Figure S11 shows the corresponding evolution of multidomain protonation under gate biases of <3 V. This progressive evolution is in

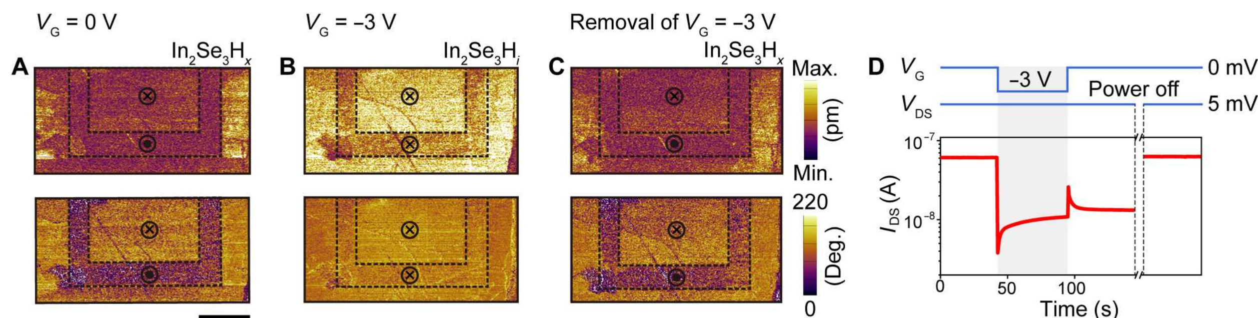

Fig. 3. Volatility of protonated ferroelectric phases. Patterned ferroelectric domains under different gate biases: (**A**) 0 V, (**B**) −3 V, and (**C**) after the removal of −3 V. At a 0-V gate bias, outer and inner boxes in (A) were written by PFM probes with DC voltages of −8 and +8 V, respectively. "⊙" and "⊗" indicate polarization pointing upward and downward, respectively. The top in (A) to (C) are PFM amplitude mappings, while the bottom are PFM phase mappings. Scale bar, 1 μm. (**D**) Dynamic current change upon applying different V_G and V_{DS}. Although the application of V_G can switch the channel current to a low level, this switching effect can be erased by removing V_{DS}, suggesting the volatile nature of protonic modulation.

line with the behaviors in Fig. 2C. Unexpectedly, after the removal of the gate bias, electric field–based proton extraction rapidly terminates but proton reservoirs in the silica substrate continuously supplement the channels with protons, consequently reversing α-$In_2Se_3H_i$ to α-$In_2Se_3H_x$ ($x > i$) phase, as revealed by PFM mapping in Fig. 3C. This behavior verifies the volatile nature of ferroelectric phase transition induced by proton injection, distinguishable from electric field–induced nonvolatility (*40*). The volatility is coincident with that of proton-induced ferromagnetic-paramagnetic phase transition (*31*).

To give insight into the volatile PFM response, we obtained dynamic drain-source currents as a function of the application and termination of gate (V_G) or read (V_{DS}) biases. Overall, a −3-V gate bias can sharply reduce the drain-source current from initial states; after the removal of this gate bias, the current increases but remains much smaller than the initial value (Fig. 3D). However, once the read bias is turned off, the drain-source current coded by a −3-V gate bias is completely erased and returns to the initial value. These electrical properties are a remarkable signature of volatility for gate-tuned protonic phases, which coincides with our PFM results. The trend in the current change—a peak and saturation currents—upon the application of a −3-V gate bias suggests that protonation can lastly reach a deprotonated plateau across the channel (i.e., barely protonated phase). This is additional clear evidence for proton-induced phase transition as observed in VO_2 (*29*, *39*). After taking away the gate bias ($V_G = 0$), metastable protonic phases relax to an energetically stable state, i.e., α-$In_2Se_3H_x$ compound. Despite a small conductance change, a reversal of α-$In_2Se_3H_x$ can occur, demonstrating the sensitivity of ferroelectric phase transitions to proton concentration/gate biases. Similar results are also demonstrated for gate tuning by positive gate biases (fig. S12).

Table 1. Comparison of gate switching voltages. FE-FET, ferroelectric field-effect transistors; FS-FET, ferroelectric semiconductor field-effect transistors; CIPS, $CuInP_2S_6$; Gr, graphene; PMN-PT, $(1-x)[Pb(Mg_{1/3}Nb_{2/3})O_3]$-$x[PbTiO_3]$.

Device structures	Gate switching voltage	Dielectric thickness	Mechanism
AlScN/MoS_2 FE-FET (*52*)	~−40 V to +20 V	100-nm AlScN	Electric field–induced polarization switching
InSe/h-BN/CIPS FE-FET (*53*)	~−4 V to +1 V	8-nm h-BN/70-nm CIPS	
PMN-PT/h-BN/Gr FE-FET (*54*)	~−24 V to +50 V	100-μm PMN-PT/50-nm h-BN	
MoS_2/CIPS FE-FET (*55*)	~−3 V to +3 V	400-nm CIPS	
In_2Se_3 FS-FET (*56*)	~−40 V to +5 V	90-nm SiO_2	
In_2Se_3 FS-FET (this work)	~−0.4 V to +0.4 V	10-nm Al_2O_3/190-nm porous silica	Proton-induced ferroelectric phase transition

Low switching voltages and polar switchability

Next, we discuss the second type of protonic α-In_2Se_3 devices with a high proton injection efficiency (Device 2; Fig. 4). Compared to Device 1 in Fig. 2, the generated gaps at the interfaces are largely reduced because channel samples in this device are almost in complete contact with the silica substrate. Possibly because of this ideal interface, abrupt changes in transfer curves are obtained as shown in Fig. 4A. For the transition from off-current to on-current, an ultralow voltage (<0.4 V) is sufficient to provide the required energy for complete protonation across the channel. As the voltage sweeps back in the other direction and changes polarity, protons are markedly driven out of the channel, creating a proton-deficient α-$In_2Se_3H_i$ phase.

To have an in-depth understanding of electrical hysteresis loops in Fig. 4A, PFM measurement was used to analyze the change in material composition. Albeit using a small gate bias (0.5 V), PFM amplitude discrepancies in Fig. 4B clearly affirm proton-induced phase transition. Furthermore, similar electrical and PFM behaviors were also detected in a separate transistor (fig. S13), which shares the same channel flake with the device used to produce the data in Fig. 4 but without bottom gate electrodes. Such a control experiment confirms the facts of proton diffusion within channel materials and proton-induced hysteresis, which rules out the electric field–induced switching. Note that the ultralow operation voltage (<0.4 V) provides an encouraging possibility of developing low-

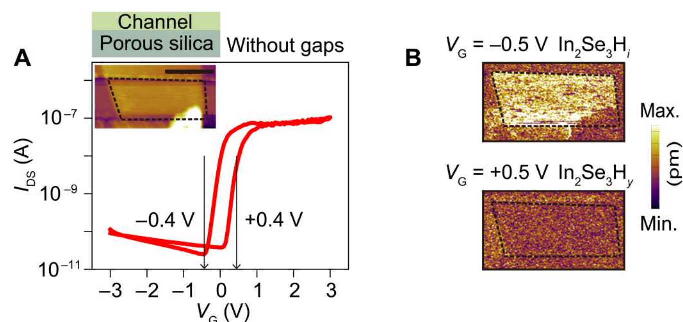

Fig. 4. Ferroelectric phase transitions with low operation voltages (Device 2). (**A**) Electrical hysteresis loops for proton-gated α-In_2Se_3 devices with ideal interfaces (i.e., no gaps between porous silica and the channel). The inset shows an AFM topographic image of a typical device, in which dashed lines highlight the device channels. Scale bar, 1 μm. (**B**) PFM amplitude mappings of the channel area [i.e., the inset of (A)] with the application of different gate biases: −0.5 and +0.5 V.

power information storage devices. Unlike ferroelectric polarization–based memory devices (see Table 1), our protonic ferroelectric transistors have competitive advantages in terms of the gate switching voltage.

Last, as indicated by the blue and red curves in Fig. 5, we used electrical hysteresis loops to uncover reversible polarization switching for barely (α-$In_2Se_3H_i$) and heavily (α-$In_2Se_3H_y$) protonated phases. Under low drain-source voltage sweeping, there is no obvious hysteresis in both α-$In_2Se_3H_i$ and α-$In_2Se_3H_y$ phases because the field magnitude is lesser than their required coercive fields (Fig. 5A). However, when drain-source voltages are increased to 5 V, an expanded hysteresis is observed with a high on/off ratio (Fig. 5B). These comparable results, in addition to theoretical predictions in Fig. 1 and multiple domain patterns in Fig. 3A, strongly demonstrate that protonated α-In_2Se_3 phases maintain switchable dipoles. The discovered polar nature is nontrivial due to the incorporation of two mutually exclusive phenomena, i.e., ferroelectricity and ion conduction, particularly at high proton concentrations.

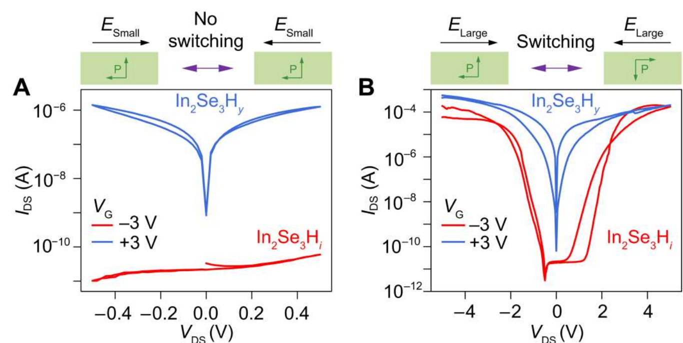

Fig. 5. Evidence for the switchability of proton-deficient and proton-sufficient phases. Electrical hysteresis loops under different gates and read biases: Drain-source voltage sweeps over (**A**) ±0.5 V and (**B**) ±5 V. Schematics on top of (A) and (B) indicate whether the switching of protonated α-In_2Se_3 phases occurs under small (E_{Small}) and large (E_{Large}) in-plane electric fields. Black arrows dictate the directions of sweeping electric fields, whereas green orthogonal arrows represent the interlocked in-plane and out-of-plane polarizations in α-In_2Se_3H compounds.

DISCUSSION

Using vdWs ferroelectric α-In_2Se_3 as a model system, we have created a multitude of metastable ferroelectric phases and demonstrated their reversible transitions by gate bias–induced proton injection. We find that the produced ferroelectric phases are volatile and polar, which can be attributed to hydrogen-stabilized α-In_2Se_3 phases with switchable dipoles. Moreover, we also demonstrate the ultralow voltage switching of ferroelectric phases (<0.4 V). We note that, despite the relatively low operation speed (29.8 ms; fig. S14), proton-induced ferroelectric phase transitions indeed feature a low operation voltage and large storage capacity (the maximum depending on the proton concentration and the resulting intermediate phases), which outperform commercial ferroelectric random access memory.

The ability to intercalate ions into vdWs ferroelectrics opens up a possible route for exploring collective physical interactions, such as the effects of charge, lattice, ion, and dimensionality. Although our calculation has predicted that the inserted protons form covalent bonds with Se atoms, the possibility of proton migration in the channels via the continuous bond-breaking and formation process remains unknown. Along this line, opportunities may emerge, such as the gate-tunable coupling of ion migration and electric dipoles, as well as their thickness-dependent effect. Furthermore, these inserted ions are envisioned to provide additional energy, during ferroelectric switching, to stabilize certain hidden phases involved with covalent bond breaking, which are barely accessible in equilibrium phase states. In addition, the insertion of ions into vdWs ferroelectrics has the potential to achieve numerous bits of information storage (fig. S15) in a single transistor cell, by finely tuning the quantity of created phases. This prospect awaits further confirmation.

MATERIALS AND METHODS

Protonic transistor fabrication

First, a 10-nm-thick Pt gate electrode (50 μm by 50 μm) was fabricated on a Si/SiO_2 substrate via electron beam lithography and metal sputtering. Then, a 10-nm-thick Al_2O_3 layer was deposited over the entire substrate using atomic layer deposition to reduce gate leakage current. Afterward, a 190-nm-thick porous silica layer, which acts as a proton reservoir, was fabricated on the Al_2O_3 layer using a previously reported method (*29*): tetraethyl orthosilicate, ethanol, deionized water, and phosphoric acid (85 weight %) were mixed in a molar ratio of 1:18:5.55:0.02, respectively, and stirred in a sealed bottle at room temperature for 1 hour; after annealing in an oven at 60°C for 2 hours, the solution was spin-coated on $Si/SiO_2/Pt/Al_2O_3$ substrates at 3000 rpm for 1 min, followed by annealing on a hot plate at 120°C for 30 min. Subsequently, α-In_2Se_3 flakes exfoliated from the parent crystal via the scotch tape method were transferred onto polydimethylsiloxane stamps. α-In_2Se_3 flakes with appropriate shapes and thicknesses were identified using optical microscopy and then transferred onto porous silica layers, right above the Pt gate electrodes, using an accurate transfer platform (Metatest E1-M). After electron beam lithography patterning and electron beam evaporation, Ti/Au (10 nm/70 nm) electrodes were deposited on the α-In_2Se_3 flakes to produce protonic transistors.

Electrical, Raman, and PFM measurements

All electrical measurements were performed at room temperature by using a Keithley 4200-SCS semiconductor characterization system equipped with source measure units. A probe station (Everbeing EB-6) was used to support these devices and connect microelectrodes with the semiconductor characterization system.

Raman spectra were collected using WITec alpha300 with a 532-nm laser and grating (1800 g/mm). The laser power density was set to ~0.3 mW to avoid damaging α-In_2Se_3 flakes. A 50× objective lens was used to monitor the Raman signals.

PFM was conducted by using Asylum MFP-3D with a probe constant of 2.8 N/m. An AC bias of 0.5 V and Dual AC Resonance Tracking mode were adopted to acquire amplified out-of-plane piezoelectric responses. During the measurements, source terminals were always grounded to reduce charge accumulation across sample surfaces. A Keithley 2636B voltage source was used to apply a DC gate bias during PFM measurements.

First-principles calculations

First-principles calculations for structural relaxation and ground state electronic structure were performed using density functional theory (*46*, *47*) as implemented in the Vienna Ab initio Simulation Package (*48*, *49*) with the projector-augmented wave method for treating core electrons. The maximal residual forces for structural relaxation were less than 0.02 eV $Å^{-1}$, and the convergence criteria for electronic relaxation was 10^{-6} eV. We used the Perdew-Burke-Ernzerhof (*50*) form of exchange-correlation functional, a plane-wave basis with an energy cutoff of 400 eV, and a Monkhorst-Pack k-point sampling of 12 × 12 × 1 for the Brillouin zone integration. The climbing image nudged elastic band method (*51*) was adopted for searching the minimum energy pathways based on the interatomic forces and total energy acquired from density functional theory calculations.

Supplementary Materials

This PDF file includes:
Supplementary Text
Figs. S1 to S15
References

REFERENCES AND NOTES

1. W. Li, X. Qian, J. Li, Phase transitions in 2D materials. *Nat. Rev. Mater.* **6**, 829–846 (2021).
2. M.-H. Zhang, L. Fulanović, S. Egert, H. Ding, P. B. Groszewicz, H.-J. Kleebe, L. Molina-Luna, J. Koruza, Electric-field-induced antiferroelectric to ferroelectric phase transition in polycrystalline $NaNbO_3$. *Acta Mater.* **200**, 127–135 (2020).
3. F. Xue, Y. Ma, H. Wang, L. Luo, Y. Xu, T. D. Anthopoulos, M. Lanza, B. Yu, X. Zhang, Two-dimensional ferroelectricity and antiferroelectricity for next-generation computing paradigms. *Matter* **5**, 1999–2014 (2022).
4. S. Barraza-Lopez, B. M. Fregoso, J. W. Villanova, S. S. P. Parkin, K. Chang, Colloquium: Physical properties of group-IV monochalcogenide monolayers. *Rev. Mod. Phys.* **93**, 011001 (2021).
5. Y. Zhou, Y. K. Zhang, Q. Yang, J. Jiang, P. Fan, M. Liao, Y. C. Zhou, The effects of oxygen vacancies on ferroelectric phase transition of HfO_2-based thin film from first-principle. *Comp. Mater. Sci.* **167**, 143–150 (2019).
6. X. Tan, C. Ma, J. Frederick, S. Beckman, K. G. Webber, The antiferroelectric ↔ ferroelectric phase transition in lead-containing and lead-free perovskite ceramics. *J. Am. Ceram. Soc.* **94**, 4091–4107 (2011).
7. M. Hoffmann, U. Schroeder, C. Künneth, A. Kersch, S. Starschich, U. Böttger, T. Mikolajick, Ferroelectric phase transitions in nanoscale HfO_2 films enable giant pyroelectric energy conversion and highly efficient supercapacitors. *Nano Energy* **18**, 154–164 (2015).
8. X. Li, T. Qiu, J. Zhang, E. Baldini, J. Lu, A. M. Rappe, K. A. Nelson, Terahertz field-induced ferroelectricity in quantum paraelectric $SrTiO_3$. *Science* **364**, 1079–1082 (2019).
9. P. Yudin, J. Duchon, O. Pacherova, M. Klementova, T. Kocourek, A. Dejneka, M. Tyunina, Ferroelectric phase transitions induced by a strain gradient. *Phys. Rev. Res.* **3**, 033213 (2021).
10. P. Chandra, G. G. Lonzarich, S. E. Rowley, J. F. Scott, Prospects and applications near ferroelectric quantum phase transitions: A key issues review. *Rep. Prog. Phys.* **80**, 112502 (2017).
11. H. Shen, J. Liu, K. Chang, L. Fu, In-plane ferroelectric tunnel junction. *Phys. Rev. Appl.* **11**, 024048 (2019).
12. X.-J. Song, T. Zhang, Z.-X. Gu, Z.-X. Zhang, D.-W. Fu, X.-G. Chen, H.-Y. Zhang, R.-G. Xiong, Record enhancement of Curie temperature in host-guest inclusion ferroelectrics. *J. Am. Chem. Soc.* **143**, 5091–5098 (2021).
13. Y. Li, Z. Liao, F. Fang, X. Wang, L. Li, J. Zhu, Significant increase of Curie temperature in nano-scale $BaTiO_3$. *Appl. Phys. Lett.* **105**, 182901 (2014).
14. A. R. Damodaran, E. Breckenfeld, Z. Chen, S. Lee, L. W. Martin, Enhancement of ferroelectric Curie temperature in $BaTiO_3$ films via strain-induced defect dipole alignment. *Adv. Mater.* **26**, 6341–6347 (2014).
15. M. Mehboudi, B. M. Fregoso, Y. Yang, W. Zhu, A. van der Zande, J. Ferrer, L. Bellaiche, P. Kumar, S. Barraza-Lopez, Structural phase transition and material properties of few-layer monochalcogenides. *Phys. Rev. Lett.* **117**, 246802 (2016).
16. Y. J. Shin, Y. Kim, S.-J. Kang, H.-H. Nahm, P. Murugavel, J. R. Kim, M. R. Cho, L. Wang, S. M. Yang, J.-G. Yoon, J.-S. Chung, M. Kim, H. Zhou, S. H. Chang, T. W. Noh, Interface control of ferroelectricity in an $SrRuO_3/BaTiO_3/SrRuO_3$ capacitor and its critical thickness. *Adv. Mater.* **29**, 1602795 (2017).
17. D. D. Fong, G. B. Stephenson, S. K. Streiffer, J. A. Eastman, O. Auciello, P. H. Fuoss, C. Thompson, Ferroelectricity in ultrathin perovskite films. *Science* **304**, 1650–1653 (2004).
18. K. Chang, T. P. Kaloni, H. Lin, A. Bedoya-Pinto, A. K. Pandeya, I. Kostanovskiy, K. Zhao, Y. Zhong, X. Hu, Q.-K. Xue, X. Chen, S.-H. Ji, S. Barraza-Lopez, S. S. P. Parkin, Enhanced spontaneous polarization in ultrathin SnTe films with layered antipolar structure. *Adv. Mater.* **31**, 1804428 (2019).
19. Z. Guan, Y. Zhao, X. Wang, N. Zhong, X. Deng, Y. Zheng, J. Wang, D. Xu, R. Ma, F. Yue, Y. Cheng, R. Huang, P. Xiang, Z. Wei, J. Chu, C. Duan, Electric-field-induced room-temperature antiferroelectric–ferroelectric phase transition in van der Waals layered GeSe. *ACS Nano* **16**, 1308–1317 (2022).
20. T. Lu, A. J. Studer, L. Noren, W. Hu, D. Yu, B. McBride, Y. Feng, R. L. Withers, H. Chen, Z. Xu, Y. Liu, Electric-field-induced AFE-FE transitions and associated strain/preferred orientation in antiferroelectric PLZST. *Sci. Rep.* **6**, 23659 (2016).
21. K. Chang, F. Küster, B. J. Miller, J.-R. Ji, J.-L. Zhang, P. Sessi, S. Barraza-Lopez, S. S. P. Parkin, Microscopic manipulation of ferroelectric domains in SnSe monolayers at room temperature. *Nano Lett.* **20**, 6590–6597 (2020).
22. G. Apachitei, J. J. P. Peters, A. M. Sanchez, D. J. Kim, M. Alexe, Antiferroelectric tunnel junctions. *Adv. Electron. Mater.* **3**, 1700126 (2017).
23. S.-C. Chang, N. Haratipour, S. Shivaraman, T. L. Brown-Heft, J. Peck, C.-C. Lin, I.-C. Tung, D. R. Merrill, H. Liu, C.-Y. Lin, F. Hamzaoglu, M. V. Metz, I. A. Young, J. Kavalieros, U. E. Avci. Anti-Ferroelectric $Hf_xZr_{1-x}O_2$ Capacitors for High-Density 3-D Embedded-DRAM,in *2020 IEEE International Electron Devices Meeting (IEDM)* (2020), pp. 28.1.1–28.1.4.
24. F. Zhuo, D. Damjanovic, Q. Li, Y. Zhou, Y. Ji, Q. Yan, Y. Zhang, Y. Zhou, X. Chu, Giant shape memory and domain memory effects in antiferroelectric single crystals. *Mater. Horiz.* **6**, 1699–1706 (2019).
25. M. F. Sarott, M. D. Rossell, M. Fiebig, M. Trassin, Multilevel polarization switching in ferroelectric thin films. *Nat. Commun.* **13**, 3159 (2022).
26. Y. Xu, Y. Yang, S. Zhao, T. Gong, P. Jiang, Y. Wang, P. Yuan, Z. Dang, Y. Chen, S. Lv, Y. Ding, Y. Wang, J. Bi, Q. Luo, M. Liu. Improved Multi-Bit Storage Reliablity by Design of Ferroelectric Modulated Anti-Ferroelectric Memory, in *2021 IEEE International Electron Devices Meeting (IEDM)* (2021), pp. 6.2.1–6.2.4.
27. P. Hou, C. Chen, B. Li, S. Zheng, J. Wang, X. Zhong, M. Liao, Mechanical manipulation of nano-twinned ferroelectric domain structures for multilevel data storage. *Adv. Funct. Mater.* **31**, 2011029 (2021).
28. J. Li, C. Ge, J. Du, C. Wang, G. Yang, K. Jin, Reproducible ultrathin ferroelectric domain switching for high-performance neuromorphic computing. *Adv. Mater.* **32**, 1905764 (2020).
29. M. Jo, H. J. Lee, C. Oh, H. Yoon, J. Y. Jo, J. Son, Gate-induced massive and reversible phase transition of VO_2 channels using solid-state proton electrolytes. *Adv. Funct. Mater.* **28**, 1802003 (2018).
30. G. Zheng, W.-Q. Xie, S. Albarakati, M. Algarni, C. Tan, Y. Wang, J. Peng, J. Partridge, L. Farrar, J. Yi, Y. Xiong, M. Tian, Y.-J. Zhao, L. Wang, Gate-tuned interlayer coupling in van der Waals Ferromagnet Fe_3GeTe_2 nanoflakes. *Phys. Rev. Lett.* **125**, 047202 (2020).

31. Z. Li, S. Shen, Z. Tian, K. Hwangbo, M. Wang, Y. Wang, F. M. Bartram, L. He, Y. Lyu, Y. Dong, G. Wan, H. Li, N. Lu, J. Zang, H. Zhou, E. Arenholz, Q. He, L. Yang, W. Luo, P. Yu, Reversible manipulation of the magnetic state in $SrRuO_3$ through electric-field controlled proton evolution. *Nat. Commun.* **11**, 184 (2020).
32. G. Chen, M. Robertson, M. Hoffmann, C. Ophus, A. L. F. Cauduro, R. L. Conte, H. Ding, R. Wiesendanger, S. Blügel, A. K. Schmid, K. Liu, Observation of hydrogen-induced Dzyaloshinskii-Moriya interaction and reversible switching of magnetic chirality. *Phys. Rev. X* **11**, 021015 (2021).
33. G. Chen, C. Ophus, A. Quintana, H. Kwon, C. Won, H. Ding, Y. Wu, A. K. Schmid, K. Liu, Reversible writing/deleting of magnetic skyrmions through hydrogen adsorption/desorption. *Nat. Commun.* **13**, 1350 (2022).
34. M. Huang, M. U. Hasan, K. Klyukin, D. Zhang, D. Lyu, P. Gargiani, M. Valvidares, S. Sheffels, A. Churikova, F. Büttner, J. Zehner, L. Caretta, K.-Y. Lee, J. Chang, J.-P. Wang, K. Leistner, B. Yildiz, G. S. D. Beach, Voltage control of ferrimagnetic order and voltage-assisted writing of ferrimagnetic spin textures. *Nat. Nanotechnol.* **16**, 981–988 (2021).
35. A. J. Tan, M. Huang, C. O. Avci, F. Büttner, M. Mann, W. Hu, C. Mazzoli, S. Wilkins, H. L. Tuller, G. S. D. Beach, Magneto-ionic control of magnetism using a solid-state proton pump. *Nat. Mater.* **18**, 35–41 (2019).
36. H. Yoon, M. Choi, T.-W. Lim, H. Kwon, K. Ihm, J. K. Kim, S.-Y. Choi, J. Son, Reversible phase modulation and hydrogen storage in multivalent VO_2 epitaxial thin films. *Nat. Mater.* **15**, 1113–1119 (2016).
37. J. Wei, H. Ji, W. Guo, A. H. Nevidomskyy, D. Natelson, Hydrogen stabilization of metallic vanadium dioxide in single-crystal nanobeams. *Nat. Nanotechnol.* **7**, 357–362 (2012).
38. C.-S. Yang, D.-S. Shang, N. Liu, E. J. Fuller, S. Agrawal, A. A. Talin, Y.-Q. Li, B.-G. Shen, Y. Sun, All-solid-state synaptic transistor with ultralow conductance for neuromorphic computing. *Adv. Funct. Mater.* **28**, 1804170 (2018).
39. X. Deng, Y.-F. Zhao, N. Zhong, F.-Y. Yue, R. Huang, H. Peng, X.-D. Tang, P.-H. Xiang, Y.-H. Chu, C.-G. Duan, Proton-mediated phase control in flexible and transparent Mott transistors. *Adv. Electron. Mater.* **6**, 1900742 (2019).
40. D. Dutta, S. Mukherjee, M. Uzhansky, E. Koren, Cross-field optoelectronic modulation via inter-coupled ferroelectricity in 2D In_2Se_3. *NPJ 2D Mater. Appl. Ther.* **5**, 81 (2021).
41. F. Xue, X. He, Z. Wang, J. R. D. Retamal, Z. Chai, L. Jing, C. Zhang, H. Fang, Y. Chai, T. Jiang, W. Zhang, H. N. Alshareef, Z. Ji, L.-J. Li, J.-H. He, X. Zhang, Giant ferroelectric resistance switching controlled by a modulatory terminal for low-power neuromorphic in-memory computing. *Adv. Mater.* **33**, 2008709 (2021).
42. F. Xue, X. He, J. R. D. Retamal, A. Han, J. Zhang, Z. Liu, J.-K. Huang, W. Hu, V. Tung, J.-H. He, L.-J. Li, X. Zhang, Gate-tunable and multidirection-switchable memristive phenomena in a van der Waals ferroelectric. *Adv. Mater.* **31**, 1901300 (2019).
43. M. Wang, X. Sui, Y. Wang, Y.-H. Juan, Y. Lyu, H. Peng, T. Huang, S. Shen, C. Guo, J. Zhang, Z. Li, H.-B. Li, N. Lu, A. T. N'Diaye, E. Arenholz, S. Zhou, Q. He, Y.-H. Chu, W. Duan, P. Yu, Manipulate the electronic and magnetic states in $NiCo_2O_4$ films through electric-field-induced protonation at elevated temperature. *Adv. Mater.* **31**, 1900458 (2019).
44. M. Wang, S. Shen, J. Ni, N. Lu, Z. Li, H.-B. Li, S. Yang, T. Chen, J. W. Guo, Y. Wang, H. Xiang, P. Yu, Electric-field-controlled phase transformation in WO_3 thin films through hydrogen evolution. *Adv. Mater.* **29**, 1703628 (2017).
45. M. Zhao, B. Gao, J. Tang, H. Qian, H. Wu, Reliability of analog resistive switching memory for neuromorphic computing. *Appl. Phys. Rev.* **7**, 011301 (2020).
46. P. Hohenberg, W. Kohn, Inhomogeneous electron gas. *Phys. Rev.* **136**, B864–B871 (1964).
47. W. Kohn, L. J. Sham, Self-consistent equations including exchange and correlation effects. *Phys. Rev.* **140**, A1133–A1138 (1965).
48. G. Kresse, J. Hafner, Ab initio molecular dynamics for liquid metals. *Phys. Rev. B* **47**, 558–561 (1993).
49. G. Kresse, J. Furthmüller, Efficiency of ab-initio total energy calculations for metals and semiconductors using a plane-wave basis set. *Comp. Mater. Sci.* **6**, 15–50 (1996).
50. J. P. Perdew, K. Burke, M. Ernzerhof, Generalized gradient approximation made simple. *Phys. Rev. Lett.* **77**, 3865–3868 (1996).
51. G. Henkelman, B. P. Uberuaga, H. Jónsson, A climbing image nudged elastic band method for finding saddle points and minimum energy paths. *J. Chem. Phys.* **113**, 9901–9904 (2000).
52. X. Liu, D. Wang, K.-H. Kim, K. Katti, J. Zheng, P. Musavigharavi, J. Miao, E. A. Stach, R. H. Olsson III, D. Jariwala, Post-CMOS compatible aluminum scandium nitride/2D channel ferroelectric field-effect-transistor memory. *Nano Lett.* **21**, 3753–3761 (2021).
53. P. Singh, S. Baek, H. H. Yoo, J. Niu, J.-H. Park, S. Lee, Two-dimensional CIPS-InSe van der Waal heterostructure ferroelectric field effect transistor for nonvolatile memory applications. *ACS Nano* **16**, 5418–5426 (2022).
54. N. Park, H. Kang, J. Park, Y. Lee, Y. Yun, J.-H. Lee, S.-G. Lee, Y. H. Lee, D. Suh, Ferroelectric single-crystal gated graphene/hexagonal-BN/ferroelectric field-effect transistor. *ACS Nano* **9**, 10729–10736 (2015).
55. M. Si, P.-Y. Liao, G. Qiu, Y. Duan, P. D. Ye, Ferroelectric field-effect transistors based on MoS_2 and $CuInP_2S_6$ two-dimensional van der Waals heterostructure. *ACS Nano* **12**, 6700–6705 (2018).
56. M. Si, A. K. Saha, S. Gao, G. Qiu, J. Qin, Y. Duan, J. Jian, C. Niu, H. Wang, W. Wu, S. K. Gupta, P. D. Ye, A ferroelectric semiconductor field-effect transistor. *Nat. Electron.* **2**, 580–586 (2019).
57. Y.-T. Huang, N.-K. Chen, Z.-Z. Li, X.-P. Wang, H.-B. Sun, S. Zhang, X.-B. Li, Two-dimensional In_2Se_3: A rising advanced material for ferroelectric data storage. *Inf. Dent.* **4**, e12341 (2022).
58. F. Xue, W. Hu, K.-C. Lee, L.-S. Lu, J. Zhang, H.-L. Tang, A. Han, W.-T. Hsu, S. Tu, W.-H. Chang, C.-H. Lien, J.-H. He, Z. Zhang, L.-J. Li, X. Zhang, Room-temperature ferroelectricity in hexagonally layered α-In_2Se_3 nanoflakes down to the monolayer limit. *Adv. Funct. Mater.* **28**, 1803738 (2018).
59. J. Xiao, H. Zhu, Y. Wang, W. Feng, Y. Hu, A. Dasgupta, Y. Han, Y. Wang, D. A. Muller, L. W. Martin, P. Hu, X. Zhang, Intrinsic two-dimensional ferroelectricity with dipole locking. *Phys. Rev. Lett.* **120**, 227601 (2018).
60. C. Cui, W.-J. Hu, X. Yan, C. Addiego, W. Gao, Y. Wang, Z. Wang, L. Li, Y. Cheng, P. Li, X. Zhang, H. N. Alshareef, T. Wu, W. Zhu, X. Pan, L.-J. Li, Intercorrelated in-plane and out-of-plane ferroelectricity in ultrathin two-dimensional layered semiconductor In_2Se_3. *Nano Lett.* **18**, 1253–1258 (2018).
61. F. Lyu, Y. Sun, Q. Yang, B. Tang, M. Li, Z.-Z. Li, M. Sun, P. Gao, L.-H. Ye, Q. Chen, Thickness-dependent band gap ofα-In2Se3: From electron energy loss spectroscopy to density functional theory calculations. *Nanotechnology* **31**, 315711 (2020).
62. M. Si, Y. Luo, W. Chung, H. Bae, D. Zheng, J. Li, J. Qin, G. Qiu, S. Yu, P. D. Ye, A Novel Scalable Energy-Efficient Synaptic Device: Crossbar Ferroelectric Semiconductor Junction, in *2019 IEEE International Electron Devices Meeting (IEDM)* (2019), pp. 6.6.1–6.6.4.
63. F. Xue, X. He, W. Liu, D. Periyanagounder, C. Zhang, M. Chen, C.-H. Lin, L. Luo, E. Yengel, V. Tung, T. D. Anthopoulos, L.-J. Li, J.-H. He, X. Zhang, Optoelectronic ferroelectric domain-wall memories made from a single van der Waals ferroelectric. *Adv. Funct. Mater.* **30**, 2004206 (2020).
64. S. Wang, L. Liu, L. Gan, H. Chen, X. Hou, Y. Ding, S. Ma, D. W. Zhang, P. Zhou, Two-dimensional ferroelectric channel transistors integrating ultra-fast memory and neural computing. *Nat. Commun.* **12**, 53 (2021).
65. M. Nogami, Y. Abe, Evidence of water-cooperative proton conduction in silica glasses. *Phys. Rev. B* **55**, 12108–12112 (1997).
66. J. Jiang, J. Sun, A. Lu, Q. Wan, Self-assembled ultralow-voltage flexible transparent thin-film transistors gated by SiO_2-based solid electrolyte. *IEEE Trans. Electron Devices* **58**, 547–552 (2011).
67. J. Godet, A. Pasquarello, Proton diffusion mechanism in amorphous SiO_2. *Phys. Rev. Lett.* **97**, 155901 (2006).
68. J. Jiang, Q. Wan, J. Sun, A. Lu, Ultralow-voltage transparent electric-double-layer thin-film transistors processed at room-temperature. *Appl. Phys. Lett.* **95**, 152114 (2009).
69. M. S. Whittingham, Lithium batteries and cathode materials. *Chem. Rev.* **104**, 4271–4302 (2004).
70. A. T. Landers, H. Peng, D. M. Koshy, S. H. Lee, J. T. Feaster, J. C. Lin, J. W. Beeman, D. Higgins, J. Yano, W. S. Drisdell, R. C. Davis, M. Bajdich, F. Abild-Pedersen, A. Mehta, T. F. Jaramillo, C. Hahn, Dynamics and hysteresis of hydrogen intercalation and deintercalation in palladium electrodes: A multimodal in situ x-ray diffraction, coulometry, and computational study. *Chem. Mater.* **33**, 5872–5884 (2021).
71. K. Hanzawa, H. Sato, H. Hiramatsu, T. Kamiya, H. Hosono, Electric field-induced superconducting transition of insulating FeSe thin film at 35 K. *Proc. Natl. Acad. Sci. U.S.A.* **113**, 3986–3990 (2016).

Acknowledgments: We thank C.-G. Duan for valuable suggestions. **Funding:** This research was supported by the ZJU-Hangzhou Global Scientific and Technological Innovation Center with a startup funding (02170000-K02013012) and the King Abdullah University of Science and Technology Office of Sponsored Research (OSR) under award numbers ORA-CRG8-2019-4081 and ORA-CRG10-2021-4665. K.L. acknowledges support from the SRC/NIST nCORE SMART center. W.H. would like to acknowledge the support by the National Science Foundation of China (grant no. 61974147). H.W. acknowledges support from the Zhejiang Provincial Natural Science Foundation of China (grant no. LDT23F04014F01). F.X. acknowledges support from the Zhejiang Provincial Natural Science Foundation of China (grant no. LDT23F04013F04). **Author contributions:** X.H. and F.X. together conceived and designed the experiments. X.H. fabricated the nanodevices and measured their electronic properties. F.X. performed the PFM characterizations. X.H. and Y.M. carried out the Raman spectra measurements. C.Z. provided the silica wafers with marks. H.W. and A.F. performed the first-principles calculations. F.X., X.H., H.W., and Y.M. analyzed the data. W.H., Y.X., B.Y., and K.L. helped improve the paper. F.X. and X.H. wrote the paper. F.X. and X.Z. supervised the project. **Competing interests:** F.X., X.H., and H.W. are inventors listed on the Chinese patent ZL202211546968.5 (granted date: 14 April 2023) held by ZJU-Hangzhou Global Scientific and Technological Innovation Center that covers a ferroelectric semiconductor device, its fabrication method, and the method to realize multiple

ferroelectric phases. All other authors declare that they have no competing interests. **Data and materials availability:** All data needed to evaluate the conclusions in the paper are present in the paper and/or the Supplementary Materials.

Submitted 26 December 2022
Accepted 19 April 2023
Published 24 May 2023
10.1126/sciadv.adg4561